sustainability

MDPI

Article

The Deformation Characteristics of the Zhuka Fault in Lancang River and Its Influence on the Geostress Field

Daru Hu [1], Tao Wen [2,3,4,*], Shuyu Wu [1], Wanying Huang [2] and Huanchun Zhu [5]

[1] Hydropower China Guiyang Engineering Corporation, Ltd., Guiyang 550081, China; hudaru_gyy@powerchina.cn (D.H.); wusy_gyy@powerchina.cn (S.W.)
[2] School of Geosciences, Yangtze University, Wuhan 430100, China; 15515007463@163.com
[3] Jiacha County Branch of Hubei Yangtze University Technology Development Co., Ltd., Shannan 856499, China
[4] Badong National Observation and Research Station of Geohazards, China University of Geosciences, Wuhan 430074, China
[5] Can-Cn Geo-digitization Technology Ltd., Wuhan 430205, China; hzhu@itasca.ca
* Correspondence: wentao200840@yangtzeu.edu.cn

Abstract: The construction of infrastructure projects such as the Sichuan–Tibet Railway and western cascade hydropower stations has led to the increasing development of ultra-long and deeply buried tunnels in an environment characterized by highly active neotectonic movement, which affects the sustainable development of ecological civilization in Tibet. However, the effects of faults resulting from tectonic activity on the distribution of geostress fields have not been systematically studied. This research focuses on the development characteristics and basic type of the Zhuka fault near the RM hydropower station, aiming to analyze the phenomenon of geostress concentration in the study area. Field investigations have revealed significant high-geostress damage on the downstream slope of the lower dam site, situated on the hanging wall of the Zhuka fault. The results indicate a correlation between these high-geostress phenomena and the Zhuka fault, suggesting the concentration of geostress within a certain range on the hanging wall and outside of the fault zone. Stress concentration primarily depends on the characteristics of fault thrusting and fault morphology. The left-lateral strike-slip and thrusting process of the Zhuka fault, combined with NNW-directed tectonic compression stress and sudden changes in fault strike, contribute to geostress concentration within a specific range of the fault hanging wall. The observed high-geostress damage to the hard rock on the valley slope results from the combined effect of construction stress concentration and fourth-order valley incision stress concentration, which influences site selection for the RM hydropower station, thereby highlighting the role of geostress concentration outside the fault zone in engineering practice. This study provides valuable insights into geostress concentration and its implications for sustainable development in the Sichuan–Tibet region.

Keywords: Zhuka fault; structural plane; geostress; numerical simulation

Citation: Hu, D.; Wen, T.; Wu, S.; Huang, W.; Zhu, H. The Deformation Characteristics of the Zhuka Fault in Lancang River and Its Influence on the Geostress Field. *Sustainability* **2023**, *15*, 13473. https://doi.org/10.3390/su151813473

Academic Editor: Maurizio Lazzari

Received: 2 August 2023
Revised: 2 September 2023
Accepted: 5 September 2023
Published: 8 September 2023

1. Introduction

In the eastern foothills of the Qinghai–Tibet Plateau, the tectonic and geological environment of the southwestern mountainous region of China is complex, with rapid crustal uplift, strong plate compression, dense active faults, diverse lithologies, and frequent strong earthquakes [1–6]. However, with gradual improvements in infrastructure, the development center of China's transportation and hydropower industries has gradually shifted to the Qinghai–Tibet Plateau [7]. Therefore, in this complex and dangerous area, a large number of ultra-long and deeply buried tunnels are under construction or planning, which inevitably brings many hazards [8–10]. High-geostress disasters, represented by rock bursts and squeezing deformations, have always been the biggest problem in deep rock excavation [11–19]. The active faults widely distributed in this area also affect the construction and normal operation of major infrastructure projects. Therefore, it is necessary to conduct research on the active faults and high geostress in this area.

To date, considerable efforts have been made to study the fault activity and the geostress in various regions [20–23]. The Qinghai–Tibet Plateau is the largest plateau in the world, with multiple active fault zones within its interior. Studying these active faults is of great significance for understanding the tectonic evolution and seismic activity of the Qinghai–Tibet Plateau. Currently, research on the active faults in the Qinghai–Tibet Plateau primarily focuses on the following four aspects [2,5]. Firstly, the seismic geological characteristics of the active faults in the Qinghai–Tibet Plateau, which are a major research topic [24]. For example, the Kunlun Fault Zone in the eastern segment of the Qinghai–Tibet Plateau is a fault zone with strong seismic activity, and its seismic geological characteristics are mainly manifested as a high strain rate, high slip rate, high stress level, and multiple large earthquakes. Secondly, the topographical and geomorphic characteristics of the active faults in the Qinghai–Tibet Plateau are also a major research focus [10]. For instance, the topographical and geomorphic features of the Kunlun Fault Zone mainly include cliffs, gorges, grabens, and alluvial fans. Thirdly, the structural characteristics of the active faults in the Qinghai–Tibet Plateau are also an important research topic [6]. For example, the structural characteristics of the Kunlun Fault Zone mainly include fault orientation, fault dip angle, fault shear, etc. Lastly, seismic monitoring and prediction of the active faults in the Qinghai–Tibet Plateau are also a major research focus [24]. For example, seismic hazard assessment and earthquake prediction can be conducted in the active fault zones in the Qinghai–Tibet Plateau by utilizing seismic monitoring data and seismological methods. The impact of active faults on the distribution of geostress is a significant research focus. For instance, the movement of active fault zones leads to changes in the stress field of the Earth's surface, resulting in an uneven distribution of surface stress. Numerical simulations of the impact of active faults on geostress are also a crucial area of study [25,26]. For example, numerical simulation methods can be employed to investigate how the movement of active fault zones affects the distribution of geostress.

The development of transportation and energy infrastructure in the Sichuan–Tibet region, such as the Sichuan–Tibet Railway and cascade hydropower stations, has led to the construction of numerous long and deeply buried tunnels. However, the influence of faults formed by tectonic movement on the distribution of geostress remains poorly understood. This knowledge gap hinders sustainable development efforts in the region, as it is essential to assess and mitigate the potential geotechnical risks associated with infrastructure projects. This study investigates the main distribution characteristics of faults near the RM hydropower station, focusing on the deformation characteristics, activity, and type of the Zhuka fault. Afterwards, the distribution characteristics of geostress near the Zhuka fault are discussed, and the influence mechanism of the Zhuka fault on geostress concentration is revealed. Finally, through numerical simulation results of geostress values near the Zhuka fault and actual measurements of the geostress, the influence of the fault on the distribution of the geostress field is verified.

2. Study Area

2.1. Location of Study Area

The research area is located in the plateau canyon zone of the northern section of the famous Hengduan Mountain in southeastern Tibet. It is a series of high mountains and deep valleys that gradually transition from an east–west orientation to a north–south orientation. The terrain is higher in the north and lower in the south, with complex landforms. Within a width of approximately 120 km from west to east, there are three deeply incised river valleys: the Nu River, Lancang River, and Jinsha River, alternating with the Taniantaweng Mountain and Mangkang Mountain. The orientation of the mountain range is basically consistent with the tectonic line. Upstream (above Mangkang), it is oriented NW, and it turns almost to SN downstream of Mangkang. The average elevation in the north is around 5200 m, with relatively gentle mountain peaks, while the average elevation in the south is generally around 4000 m, with steep mountain slopes and a general height difference of more than 2000 m from the river valley to the mountain top, forming a deeply incised area of high mountains. According to the geomorphic regionalization map of China, the geomorphic classification of the RM hydropower station is the Hengduan Mountain of the southern part of the Tibetan–Dian–Qian region.

Figure 1 shows the larger scale fault in the middle dam site. In addition to the Zhuka fault, the largest fault in the middle dam site is the Zhuka Secondary Fault, which is consistent with the Rongqu Gully Fault and its upstream section. This fault starts to separate around the mouth of the Rongqu gully area, and belongs to the secondary fault derived from the Zhuka fault.

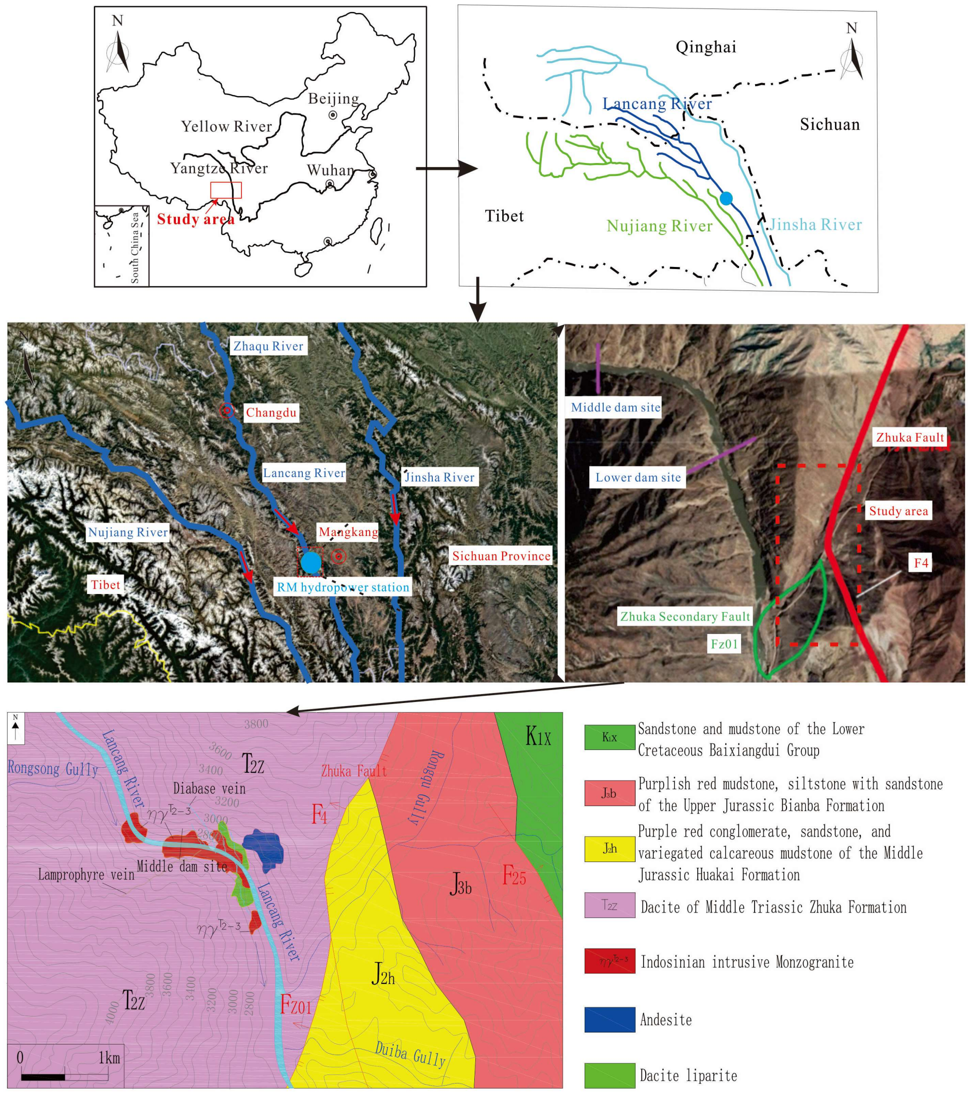

Figure 1. Location of study area and distribution geological diagram of igneous rock in the dam site area (modified from [6]).

2.2. Material Composition

The stratigraphic distribution at the middle dam site is relatively concentrated. Apart from the Quaternary system, the main distribution is the Middle Triassic Zhuka Formation (T2z). This formation includes volcanic rocks such as rhyolite, tuff, and andesite, as well as granite rocks such as fine-grained granites containing biotite and porphyritic diorite. A geological map of the distribution of magmatic rocks in the middle dam site is shown in Figure 1. Rhyolite is the main rock type in the middle dam site, and is widely distributed with a large thickness. Various alterations have occurred in the rhyolite, including the chloritization of hornblende, the potassium feldsparization and sericitization of plagioclase, and later silicification. In addition, the rhyolite also exhibits various alteration types, including kaolinization, carbonate alteration, and iron impregnation. The granite mainly consists of porphyritic diorite and medium- to fine-grained monzogranite, with a distribution range lower than that of the rhyolite. Most of these can be seen in the middle and low elevations on both sides of the axis of the dam. The granite is located in the lower part of the deeply incised river valley, on the axis of the dam, with the left bank distributed roughly below an altitude of 2870 m and the right bank distributed below an altitude of roughly 2850 m.

2.3. Distribution of Main Faults

The engineering area has a complex geological background and strong tectonic deformation. It is located in the eastern part of the Qinghai–Tibet Plateau and is an important component of the famous Tethyan tectonic domain, located in the eastern segment of the Alpine–Himalayan giant mountain system between the north and south continents. The main structures in the near-field area are folds and faults. There are four major folds in the area, including the Taya anticline, Jiaka anticline, Qinggang syncline, and Dengba overturned anticline, as shown in Figure 2. The fault structures in the near-field area are well developed, mainly consisting of five nearly SN~NW-oriented faults from west to east, including the Chalangka fault (F1), Jiaka fault (F2), Jiaoba Mountain fault (F3), Zhuka fault (F4), and Laoran fault (F5). The latest activity of these faults mainly occurred in the early-to-middle Pleistocene, and they have been relatively stable since the late Pleistocene.

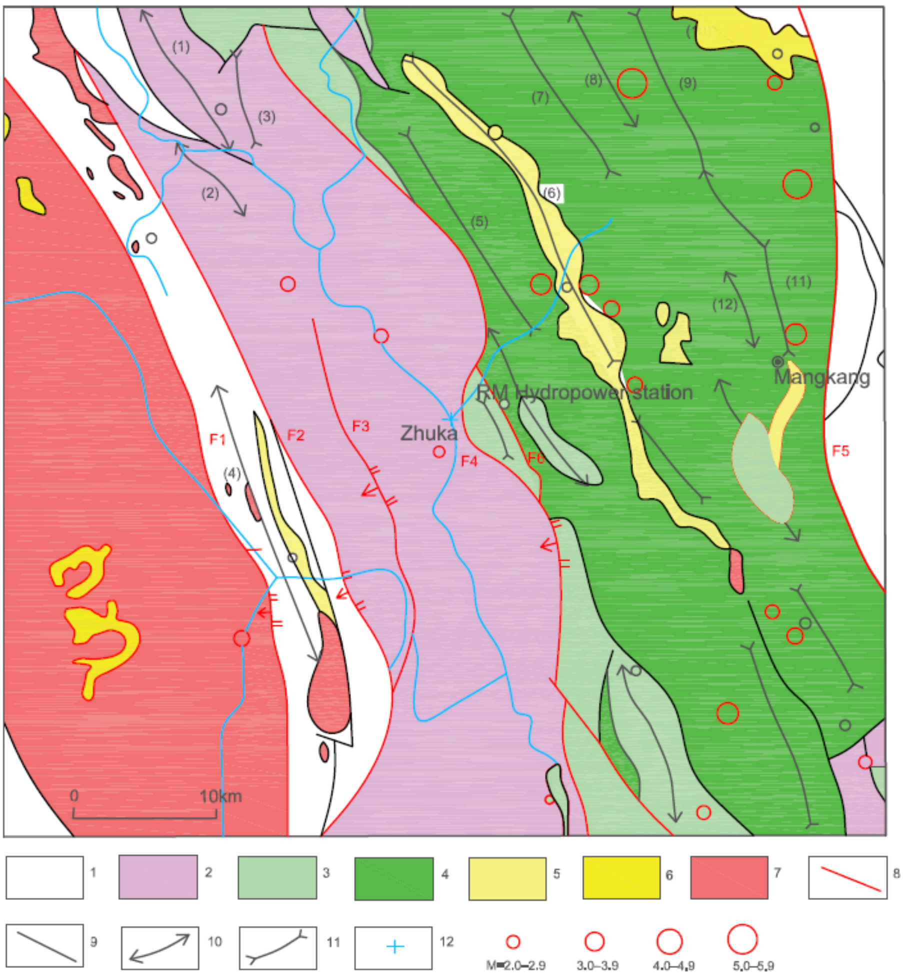

Figure 2. Structural outline of the near-field area of RM hydropower station, 1: Pre-Triassic; 2: Triassic system; 3: Jurassic system; 4: Cretaceous system; 5: Paleogene and Neogene; 6: Quaternary system;

7: Intrusive rock mass; 8: Regional main fault; 9: Secondary fracture; 10: Anticline; 11: Syncline; 12: Site; F1: Chalangka fracture; F2: Jiaka fracture; F3: Jiaoba Mountain Fault; F4: Zhuka fault; F5: Laoran Fault. In figure, the capital letters M in the legend represent earthquake magnitudes.

The main faults in the region are oriented in the N-NW to nearly N-S direction and NW to W-NW direction, followed by those in the N-E to N-NE direction. These faults differ significantly in their tectonic attributes, scale, activity periods, and strength. The N-NW to nearly N-S-oriented faults are the main faults in the area, with large scale and segmented activity. The NW to W-NW-oriented faults are also large in scale, some of which exhibit characteristics of deep and major faults, mostly reverse and strike-slip faults. These faults have experienced several earthquakes with magnitudes greater than or equal to 7, particularly during different periods of the Quaternary, especially the late period.

3. Case Study

3.1. Basic Characteristics of the Zhuka Fault

The Zhuka fault (F4), also known as the Lancang River Fault, is located in the central near-field area and east of the Lancang River, and runs through the entire area in a gentle wave-like pattern. The overall trend of the fault is NNW (NW in the northern section, and nearly SN in the southern section) with a SW dip angle of 65°, and its length in the near-field area is approximately 60 km, with the nearest distance to the dam site being 1.8 km. The fault developed between the Triassic and Jurassic–Cretaceous periods, with the southwestern block composed of volcanic rocks from the Middle Triassic Manghuai Formation, thrusting over the Jurassic–Cretaceous red beds on the northeastern block. The fault zone exhibits compressional and brecciated zones, mylonitic rocks, fault gouge, and slickensides, with the fault gouge being cemented by calcite. The slickensides on the fault plane indicate reverse faulting, with local development of overturned and dragged minor folds. The Zhuka fault is a long-term active reverse fault with a dextral strike-slip motion. It appears as a gentle wave pattern on the west side of the RM hydropower station and a westward convex arc in the area of the Rongqu gully. On the left bank of the Rongqu gully to the west of RM hydropower station, the fault has a dip angle of 20°/SE∠50° and a breccia zone width of 5–10 m, as shown in Figure 3. In the area of the Rongqu gully downstream of the RM dam site, the fault trends 315° with a dip angle of 80° to the northeast. The gravelly sand layers and pebble gravel layers of the T3 terrace overlying the fault are not displaced, and the bottom gravelly sand layer of the cover layer has been dated by thermoluminescence to (89.35 ± 82.64) ka, indicating no evidence of fault activity since the late Pleistocene.

3.1.1. Distribution Characteristics of the Zhuka Fault

The Zhuka fault in the site area is characterized by the volcanic rocks from the Middle Triassic Zhuka Formation on the hanging wall and the Jurassic Huakaizuo Formation on the footwall, consisting mainly of light gray diorite and purple-red sandstone, siltstone, limestone, and bioclastic limestone, respectively. The former was thrust over the latter, forming a distinct red-white boundary on the topography that clearly shows the existence of the fault zone, as shown in Figure 3.

In the lower dam site area, the fault zone protrudes westward in an arc shape. Based on the variations in structural characteristics, the fault can be divided into three segments. The first segment is the PDF21-PDF18 segment, which is located on the right bank of the Rongqu River and trends NNE. The second segment is the PDF18-PD23 segment, which follows the Rongqu River and trends nearly SN. The third segment is the PDF17-Duiba gully segment, which is distributed on the left bank of the Rongqu River and trends NNW, with steep dips ranging from NWW to WSW (generally 70–80°), and with some segments showing reverse dips.

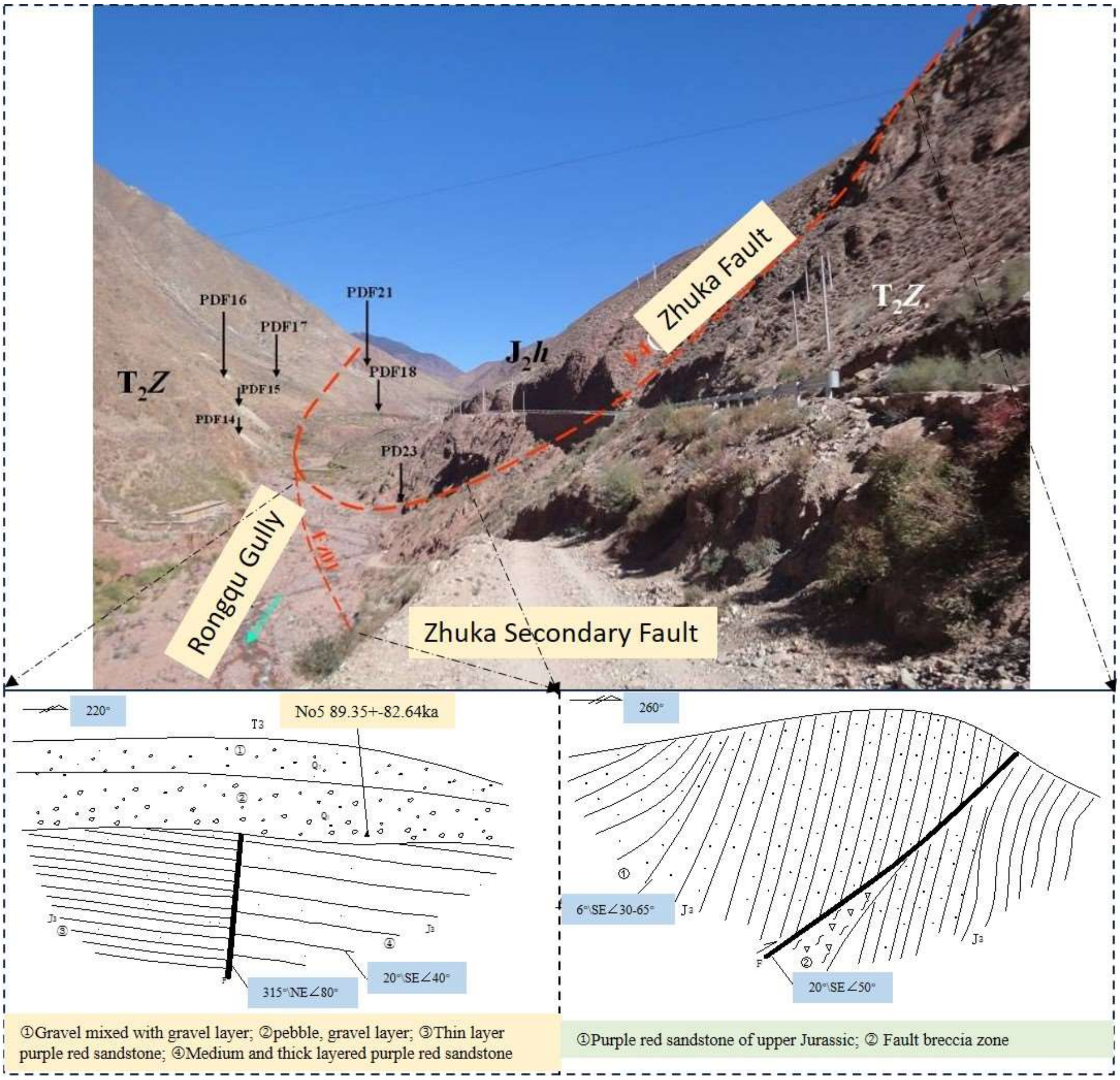

Figure 3. Distribution characteristics of the Zhuka fault and fault profiles.

3.1.2. Deformation Characteristics of the Zhuka Fault

The location of the main fault plane and the width of the main deformation zone in the Zhuka fault are further constrained by surface outcrops, underground caverns, and drilling engineering. The horizontal depth of the PDF21 adit is 136 m, with a 50 m-long strong deformation zone, while the PDF18 adit has a strong deformation zone greater than 17 m and a weak deformation zone of 77 m. The PD23 adit has a horizontal depth of 119 m, with an 86 m long strong deformation zone and a weak deformation zone of 24 m.

(1) Deformation characteristics at PDF18 adit

The PDF18 adit is located at the spillway channel slope elevation of the lower dam site of the RM hydropower station, with a tunneling depth of approximately 283 m. The lithology consists of deep gray to grayish-red mylonitized diorite and potassic diorite from the Middle Triassic Zhuka Formation (T2z), which are commonly severely altered. Nine brittle faults have mainly developed in this cavern, with a fault breccia zone width ranging from 2 cm to 60 cm. The fault breccia zone is dominated by tectonic breccia, and breccia, brecciated tuff, and fault gouge are also well developed. Some fault planes show slickensides and steps.

In Figure 4, the largest secondary fault F4-2 on the main fault plane of the Zhuka fault is developed at the 100 m point of the PDF18 adit, with a length of more than 100 m along the sub-tunnel. The fault plane is smooth and flat, with a strike of 290° and a dip of 55°. A white and yellow fault gouge of 3–5 cm and breccia of 0–50 cm have developed on the fault plane. Slickensides and steps are observed on the fault plane, indicating that the fault is a positive fault. The formation of positive faults indicates that the Zhuka fault has multiple active characteristics. In Figure 4, the F3 fault developed at a depth of 142 m in the PDF18, with a fault breccia zone of 20–50 cm. Tuffaceous breccia and brecciated tuff of 20–30 cm and fault gouge of 3–5 cm developed inside. The fault plane is straight and smooth, with a strike of 296° and a dip of 54°. Slickensides are observed on the fault plane, indicating a dextral strike-slip with reverse motion. In Figure 4, the F7 fault is developed in a well-preserved diorite body at a depth of 186 m in the PDF18. The fault breccia zone is about 3 m wide, with tectonic lenses developed inside. A fault gouge is developed on both the upper and lower boundaries of the fault plane. The strike of the upper boundary is 280° and the dip is 55°, with a few millimeters of fault gouge and 10 cm of brecciated tuff. The strike of the lower boundary is 262° and the dip is 54°, with fault gouge ranging from a few millimeters to 1 cm and 3–5 cm of brecciated tuff. Slickensides are observed on the fault plane, indicating a dextral strike-slip with reverse motion. In addition, according to the tectonic lenses developed in the fault zone, the F7 fault has a reverse component, indicating that it is a dextral strike-slip reverse fault.

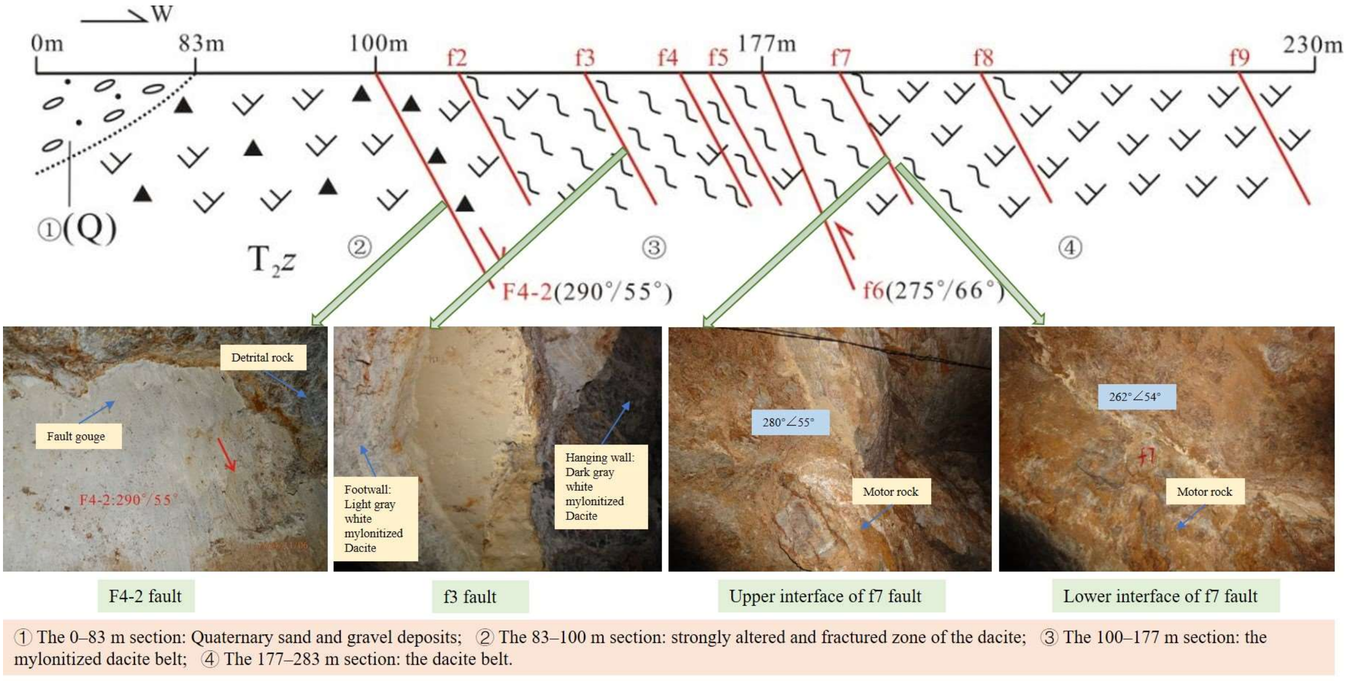

Figure 4. Schematic diagram of the PDF18 adit section in the right bank of Rongqu River and the exposed faults.

(2) Deformation characteristics at PD23 adit

In Figure 5, the PD23 adit located on the left bank of the Rongqu River provides a complete exposure of the Zhuka Fault Zone, clearly revealing deformation, zonation, and alteration features. The PD23 is 155 m deep, with the main fault plane located at a depth of 18.8 m, steeply dipping to the SW (238°∠78°). The hanging wall mainly consists of mylonitized diorite and potassic diorite from the Middle Triassic Zhuka Formation (T2z), while the footwall is composed of black calcareous and argillaceous tectonic schist and a purple-red conglomerate containing pebbles and sandstone from the Middle Jurassic Huakaizuo Formation (J2h). Based on the intensity of deformation, three deformation zones can be roughly distinguished: the hanging wall weak deformation zone before 18.8 m (F4), dominated by ductile deformation with superimposed brittle deformation; the strong deformation zone from 18.8 m to 104 m, with abundant secondary faults, development of shale–limestone cleavage and tectonic lenses, and obvious fracturing and carbonation of the limestone; and the weak deformation zone from 104 m to 128 m, namely the fault-affected zone, where shale and limestone also exhibit tectonic lenses and cleavage, but the deformation intensity and alteration are significantly reduced. After 128 m, the rock is basically intact, and the deformation is very weak.

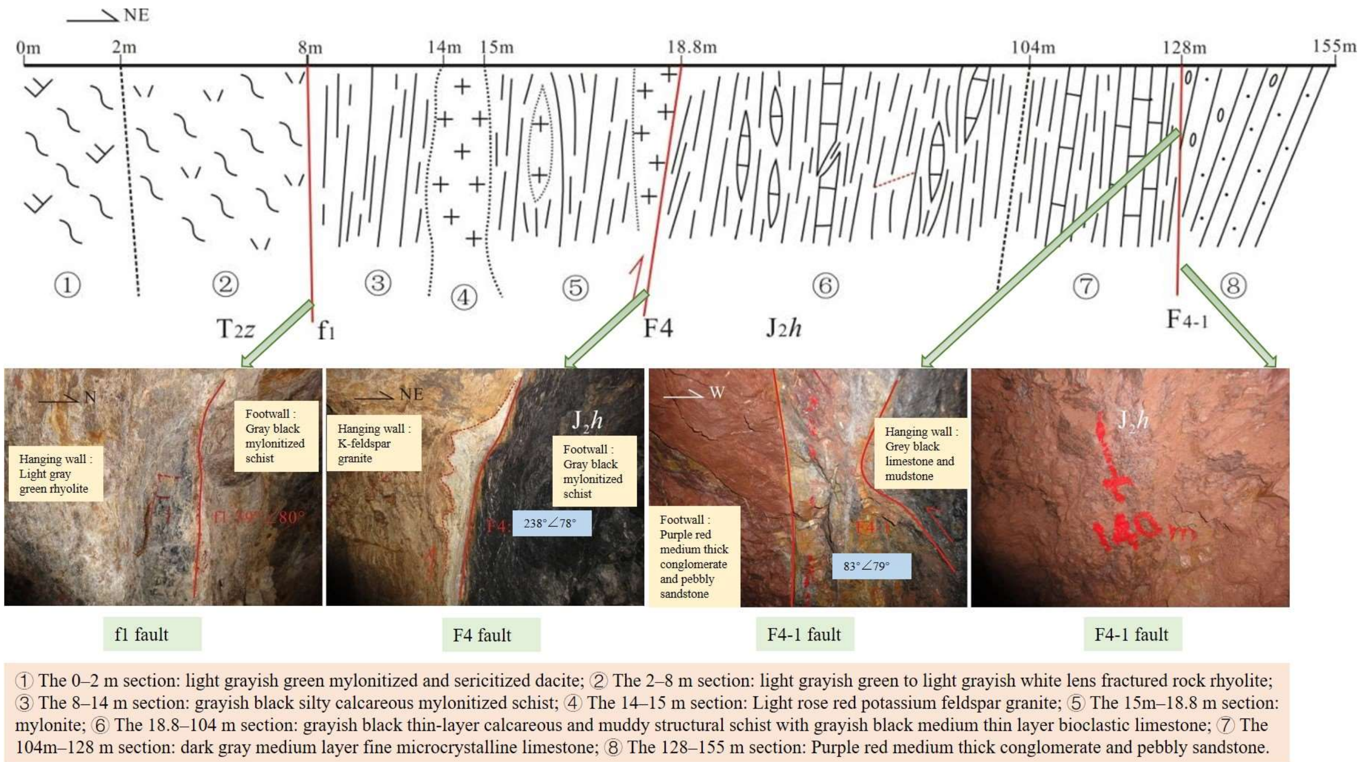

Figure 5. Schematic diagram of PD23 adit section on the left bank of Rongqu River and the exposed faults.

In Figure 5, at the 8 m point in PD23 adit, the F1 fault is developed, with a trend of 39° and a dip of 80°. The two sides of the fault are light gray-green rhyolite and gray-black mylonitized slate. At the 18.8 m point, the main fault plane of the Zhuka fault, F4, is developed, as shown in Figure 5, trending NW-SE, dipping to 238°, and dipping at 78°. The fracture zone is about 5–40 cm wide, all caused by the deformation of the hanging wall intrusive granodiorite, developing gray-white granite breccia (40 cm) and clastic breccia (10–30 cm), with obvious orientation and traction deformation at the edge of the fracture zone, indicating that the F4 fault is a reverse fault. In Figure 5, at the 128 m point in PD23 adit, the F4-1 fault is developed, with the hanging wall composed of gray-black middle-layered limestone and thin-layered calcareous shale, and the footwall composed of purple-red medium-thick conglomerate and conglomeratic sandstone. The width of the fracture zone is about 30 cm, mainly formed by the deformation of the footwall rock. A large number of cleaved breccia, smooth cleavage surfaces, and lens-shaped calcite veins are developed inside. Scratches and slickensides are observed on the cleavage surfaces, and the surface exhibits an extremely strong silky luster of muscovite film. The dip of the F4-1 fault plane is 83°∠79°, with weak traction structures observed at the boundary of the fracture zone. In addition, scratches are developed in the fracture zone at 81°∠53°, plunging 45° E, indicating that the fault is a sinistral strike-slip reverse fault.

3.1.3. Activity of the Zhuka Fault

Based on further investigations of the site area, the main evidence for the inactivity of the Zhuka fault can be summarized as follows:

(a) No structural landforms are observed along the fault zone, except for the section along the Rongqu River where the fault is developed. The fault does not show any continuous linear structural features or active tectonic geomorphic signs, as shown in Figure 6a,b.

(b) No moderate to strong earthquakes have occurred along the fault zone, indicating no activity.

(c) No hot springs have been found along the fault zone, indicating no geothermal activity.

(d) No disturbance, folding, or faulting in the Neogene and Quaternary strata in the overlying and adjacent areas and no deformation was observed in the I-III terraces of the Rongqu River, as shown in Figure 6c,d. The III terrace in the area is over 100,000 years old, indicating that the Zhuka fault has been inactive since the Late Pleistocene. A reliable particle measurement method can be used to obtain the 3D particle size and shape of the pebbles [27].

(e) In Figure 7a, quartz morphology scanning results of the clastic materials from the main fault (F4) of the Zhuka fault at the PD23 adit site show that there is no shell-like quartz or sub-shell-like quartz, and that the main type of quartz is fish scaly and mossy (50%). The remaining types of quartz are bell and worm-like (35%), pitted and coral-like (6%), and peel-like (9%). In Figure 7b,c, there is a large distribution of quartz in the shape of moss and fish. In Figure 7d, there is a large distribution of quartz in the shape of bell. This indicates that the quartz is mainly derived from medium-to-deep weathering (scaly and mossy), reflecting the characteristics of Late Neogene to Early Pleistocene activity. Since the Middle Pleistocene, the Zhuka fault has been inactive.

(f) Radiometric dating results of various fault sections all indicate an age of over 100,000 years. As shown in Table 1, radiocarbon dating of the fault clay was conducted at 20 m, 108 m, and 120 m along the PD23 adit site, with ages of (186 ± 18) ka, (333 ± 50) ka, and (215 ± 268) ka, respectively, indicating that the fault was active during the Middle to Late Pleistocene. The electron spin resonance (ESR) ages of the main fault (F4) at the 18.8 m and secondary fault at the 128 m points of the PD23 adit site were (21.55 ± 2.0) ka and (13.39 ± 0.80) ka, respectively, indicating that the Zhuka fault has been inactive. The ESR ages of typical faults, such as PDF14-50m-f6, PDF16-113m-f4, and PDF18-100m-F4-2, were 75.03 ± 7.0 ka, 10.87 ± 0.55 ka, and 10.70 ± 0.50 ka, respectively, all indicating that the fault has been inactive.

Table 1. ESR dating experiment data of faults in the lower dam site of the RM hydropower station.

Fault Name and No.	Paleodose (Gy) Annual Dose (mGy)	Uranium Content (mg/g)	Thorium Content (mg/g)	Potassium Content (%)	Age (Ten Thousand Years)
PD23-8m-F4	1946.00 9.03	3.96 ± 0.30	11.02 ± 1.00	5.24 ± 0.30	21.55 ± 2.0
PD23-128m-F4-1	1201.23 8.976	8.87 ± 0.80	24.36 ± 2.40	3.62 ± 0.35	13.39 ± 0.80
PDF14-50m-f6	6412.03 8.55	3.20 ± 0.30	9.63 ± 1.00	5.28 ± 0.50	75.03 ± 7.0
PDF16-113m-f4	1426.28 13.12	10.45 ± 1.00	30.45 ± 3.00	5.49 ± 0.50	10.87 ± 0.55
PDF18-100m-F4-2	936.36 8.756	8.07 ± 0.80	22.86 ± 2.20	3.76 ± 0.35	10.70 ± 0.50

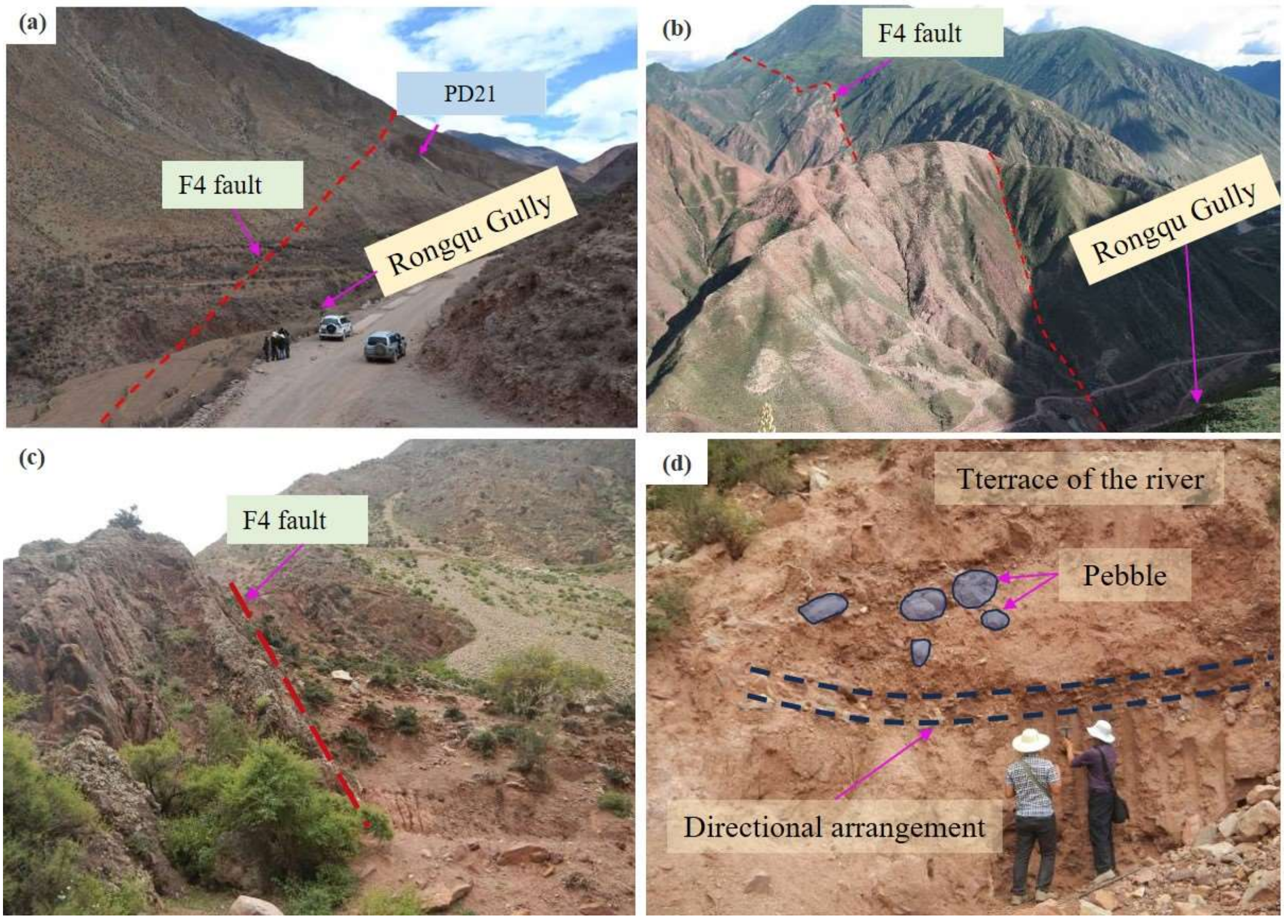

Figure 6. Landform of the Zhuka fault in the site area: (**a**) North extension of the Rongqu gully; (**b**) South extension of the Rongqu gully; (**c**,**d**) Photos of the Zhuka fault on the west side of Duiba village.

3.1.4. Basic Type of the Zhuka Fault

The dislocation characteristics of the Zhuka fault reveal the following features of tectonic activity in the dam site area:

(a) In the early stage, marked by the formation of the Zhuka fault, the tectonic movement in the area was dominated by the compressive and thrusting action on the Zhuka fault, which is consistent with other structural features such as deformation and folding in the underlying sedimentary rocks. The PDF18 adit site, located on the hanging wall of the Zhuka fault, reveals fault compression phenomena characterized by a wave-like undulating fault surface and near-vertical scratches, as shown in Figure 8a.

(b) The bending section of the Zhuka fault, namely the Zhuka secondary fault, formed at the same time as the Zhuka fault but slightly later, maintained its compressive and thrusting characteristics and also experienced right- and left-lateral strike-slip movements, with the latter being relatively weaker. The near-horizontal scratches and step-like features on the friction surface, as shown in Figure 8b, indicate that the fault initially experienced right-lateral strike-slip and later left-lateral strike-slip, with the former being more common and stronger.

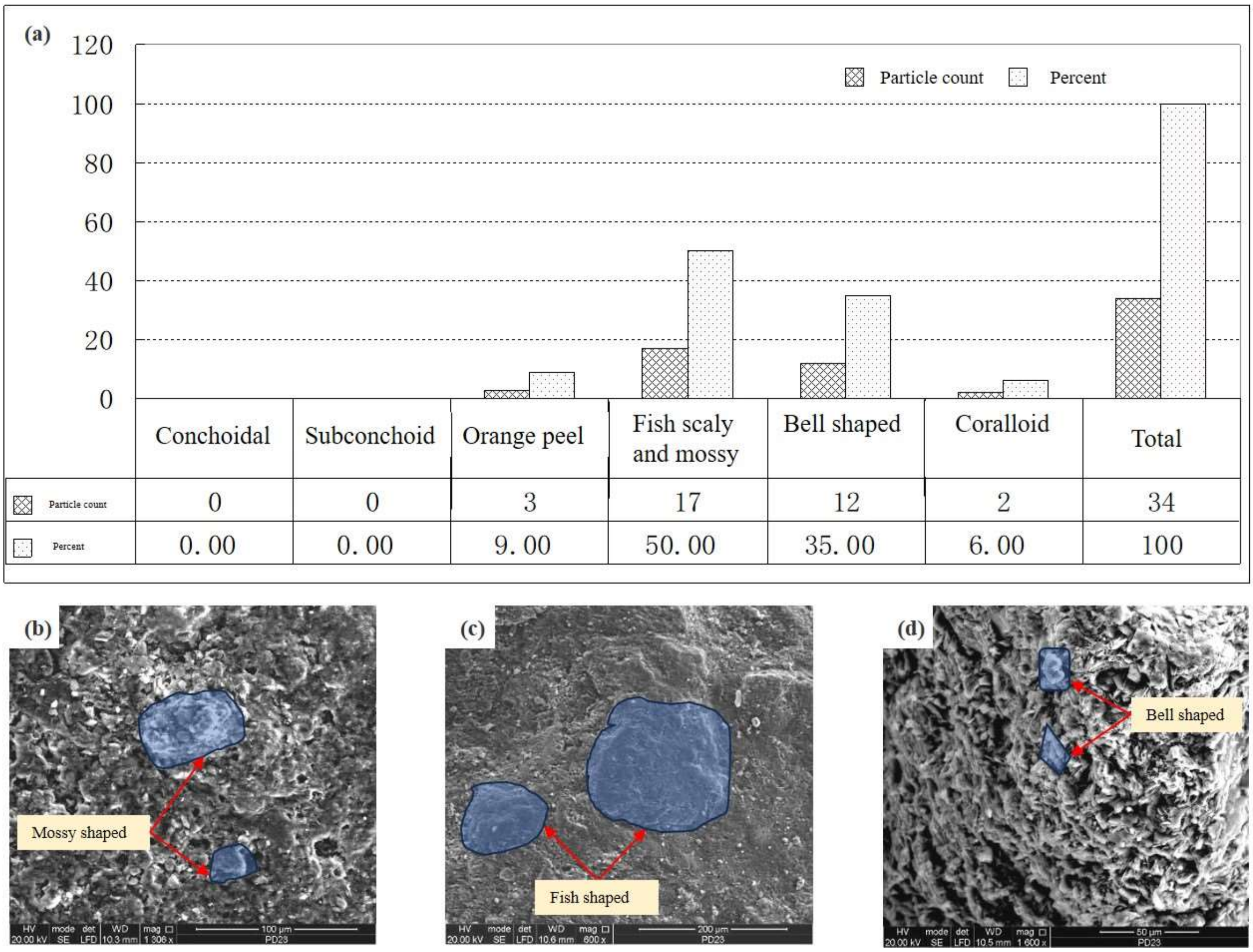

Figure 7. Distribution histogram of quartz morphology types in the Zhuka fault, and their quartz morphology in the PD23 adit: (**a**) Distribution histogram; (**b**) moss-shaped; (**c**) fish-shaped; (**d**) bell-shaped.

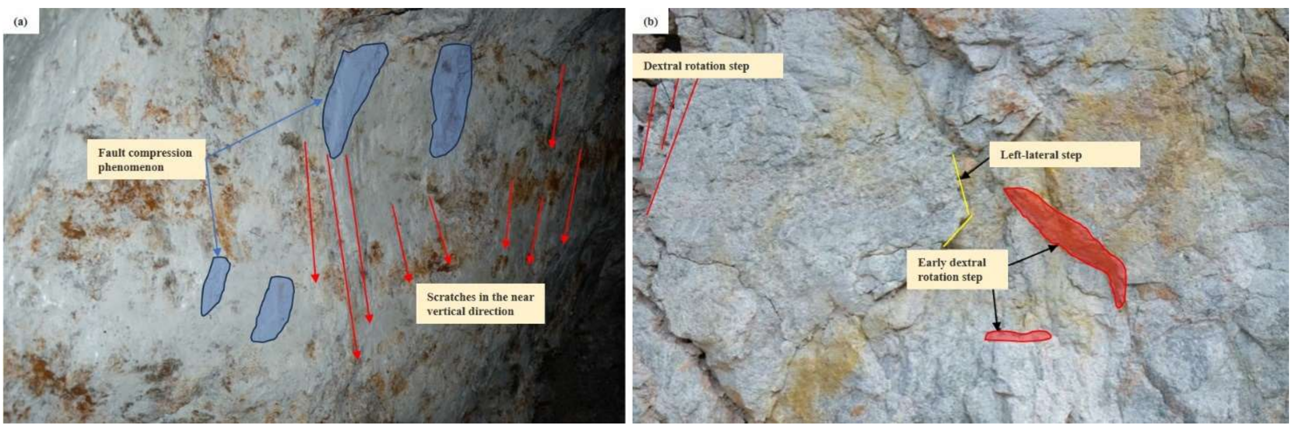

Figure 8. Extrusion characteristics of (**a**) Zhuka main fault and (**b**) Zhuka secondary fault.

In terms of tectonic activity, the compressive action was the strongest in the early stage, forming the main structural features and fault characteristics. The degree of right-lateral strike-slip that followed was much weaker, but some small-scale derivative structures can still be observed along the bending section of the Zhuka fault. Left-lateral strike-slip, on the other hand, is an expression of continuously decreasing tectonic activity. Although it did not form widespread structural phenomena, it was enough to change the stress state of the tectonic system, but the stress value was relatively low and did not reach the degree of widespread rock cracking or obvious deformation. However, this relatively weak left-lateral strike-slip characteristic in the later stage clearly indicates a change in the characteristics of the tectonic stress field, which may have affected the distribution characteristics of the present-day stress field. It is likely that the present-day stress field is the result of the evolution and transformation of the stress field under the influence of the "left-lateral strike-slip" tectonic stress field during the valley's formation.

3.2. Geostress Analysis

3.2.1. The Geostress Concentration Phenomena

Due to the historical formation of the Zhuka fault and subsequent influences from valley evolution, the section of the river located downstream of the dam site is mainly characterized by an increase in stress ratio. The influence of the bending section of the Zhuka fault results in even stronger stress concentration and more prominent stress values downstream of the dam site, particularly at the mouth of the Rongqu gully. Figure 9a shows the observed anomalies in geostress and their corresponding locations, which are summarized as follows. In Figure 9a, Mark 1 located in the area downstream of the dam site represents anomalous shear and compression on structural planes; it mainly reflects the concentration of tectonic stress and may be related to later valley evolution. Mark 2 is located on the right bank at a low elevation; this is a typical result of stress concentration in the valley, but it also reveals a slightly higher horizontal (tectonic) stress level in this area before the valley incision. Mark 3 is observed on the Rongqu ridge; this phenomenon shows greater influence from tectonic activity. Mark 4 and Mark 5 are typical results of stress concentration from tectonic activity. The former shows small-scale structural fractures, and the dense distribution and curved shape of the small joints reveal a different genesis environment from the general tectonic conditions.

Figure 9b shows the observed fracture phenomenon in the inlet section of the PDF14 adit at downstream of the dam site, which has similarities with the fractures in some fault zones. However, the fracture characteristics at this location do not show the results of tectonic activity, but rather the historical yielding of rock masses caused by stress concentration in the deeply incised riverbed (near the foot of the right bank slope).

Figure 9c shows the corresponding fracture characteristics of the stress anomaly locations mentioned above (④ in Figure 9a). Dense structural joints are developed in hard dacite, and the geometric shape of these small joints is particularly noteworthy, showing sharp curvatures with lengths mostly in the range of several meters.

Figure 9d shows observations made at the PDF03 site, where steeply inclined structural planes begin to taper off at the exposed adit location. At the end of the structural plane, dense shear fractures are observed, indicating the extension of steeply inclined structural planes and the manifestation of rock failure caused by high geostress under the conditions at the time.

Figure 9e shows the state of structural planes exposed by excavating the high-level slope on the downstream left bank of the dam site. The surfaces exhibit prominent shear displacement along the joint surface, and some areas even show thin-sheet features, which are typical manifestations of shear failure caused by high geostress. The scratches on the steeply inclined joint surfaces reveal the characteristics of horizontal displacement, which have a similar genesis mechanism to the analysis results for the shear failure observed at PDF03. The bending of tectonic stress caused by the Zhuka fault intersects with the structural plane at a small angle in the downstream direction, resulting in an increase in stress values. In a certain stage of valley incision, the normal stress decreases, leading to an increase in shear stress and the formation of strike-slip deformation.

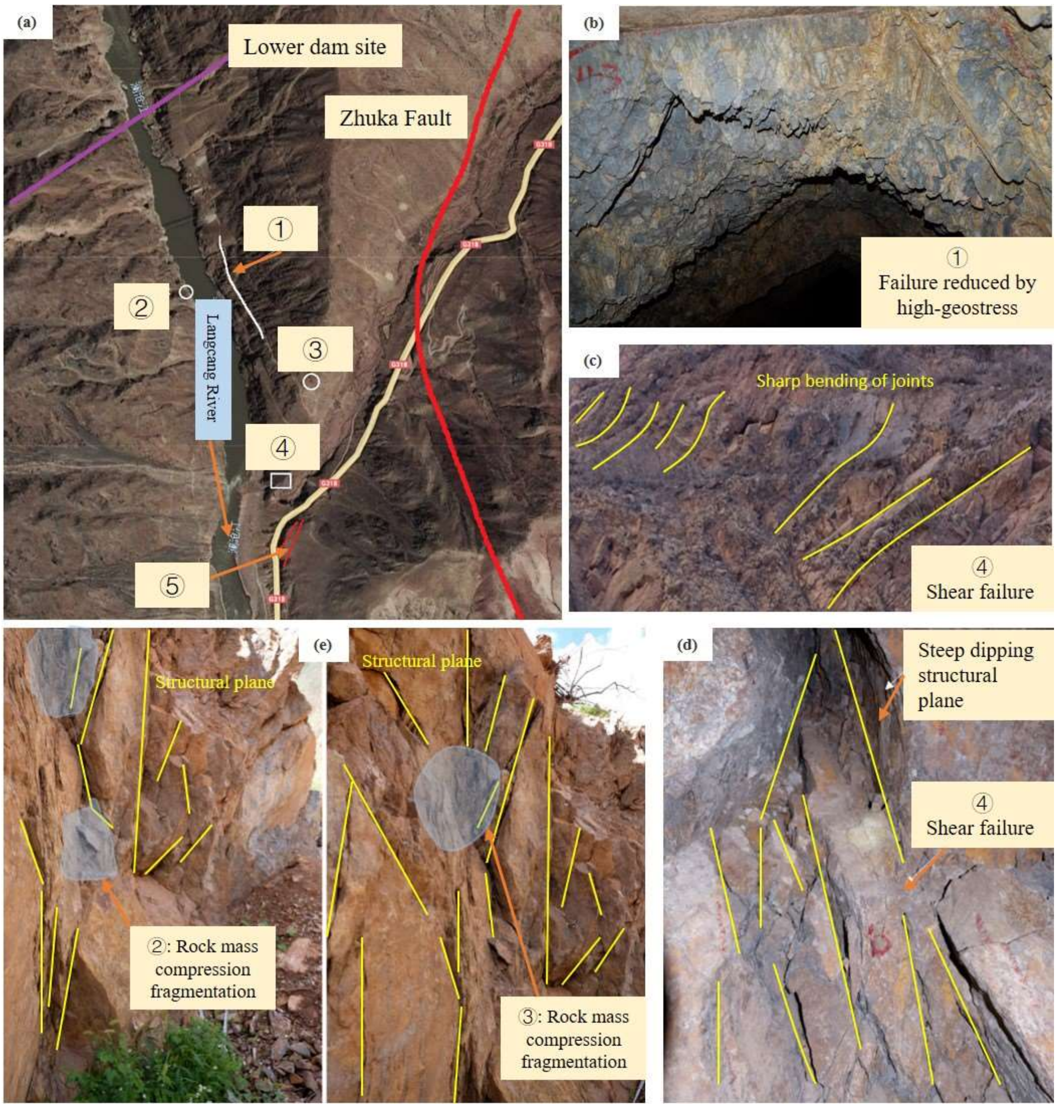

Figure 9. Fracture phenomena observed around the lower dam site: (**a**) Observed locations of geostress concentration; (**b**) Fracture phenomenon in the entrance section of the PDF14 adit; (**c**) Fracture phenomenon in the intersection area of Rongqu gully and Langcang River; (**d**) Shear failure phenomenon of the PDF03; (**e**) Weathering of rock mass and compression fragmentation in the downstream section of the left bank of the lower dam site. Note: ①, structural plane compression dislocation; ② and ③, rock mass compression fragmentation; ④, shear failure reduced by compression; ⑤, widening of fault zones.

3.2.2. The Geostress Simulation

The numerical calculations in this study were conducted using FLAC3D software. The boundary conditions employed in the computational analysis were as follows. (a) The model bottom was subjected to a z-direction constraint, i.e., normal constraint; (b) all four sides of the model were constrained in the x and y directions, while the z direction was left unconstrained; and (c) the model top was left unconstrained. The rock mass and fault were simulated using solid elements in the computational analysis, with the fault represented by thin-layer solid elements. The constitutive model for the solid elements was set as a strain-softening model, and the specific material parameter values are listed in Table 2.

Table 2. The specific material parameter values for simulation.

Type	c (MPa)		φ (°)		G (GPa)	K (GPa)	Critical Plastic Strain
	Peak Point	Residual Point	Peak Point	Residual Point			
Rock mass	5.4	2.7	45	50	6.3	10.0	0.003
Fault	1	0.5	16	20	0.5	1.1	0.004

Figure 10 shows the geological phenomena caused by geostress anomalies observed during the field investigation at the dam site. For comparison, the distribution of the numerical simulation of the geostress field caused by the Zhuka fault (before valley evolution) is shown in the right figure.

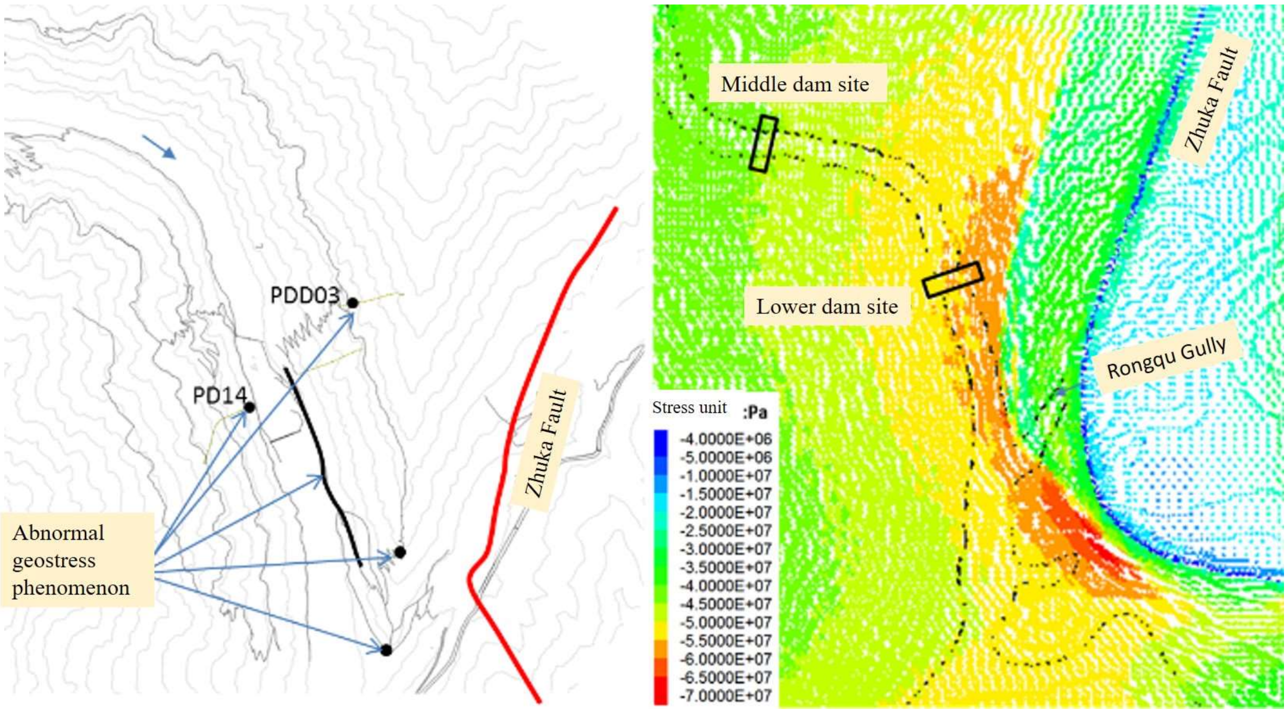

Figure 10. The observed location of geostress and the corresponding early geostress simulation results.

Five geological phenomena caused by geostress were observed at the site, and their basic understanding is summarized as follows:

(a) The strongly sheared structural plane in the PDF03 tunnel section is believed to be the result of further modification of valley evolution after the influence of the Zhuka fault, with the latter having a more prominent direct effect.
(b) The low-level slope is the overall result of the joint effects of tectonic stress anomalies and valley incision.
(c) In the PDF14 inlet section, the rock mass yielded due to the historical stress concentration in the riverbed, which was then uplifted and relaxed.
(d) On the Rongqu ridge, the joint effects of local tectonic stress anomalies (concentration) and valley incision may have played a more important role in causing tectonic anomalies.
(e) At the mouth of the Rongqu gully, the joint effects of local tectonic stress anomalies (concentration) were the main cause.

The outer side of the sharp bend of the Zhuka fault at the Rongqu ridge and the mouth of the Rongqu gully are the sites where the fault movement causes a sharp concentration of stress, providing the conditions for localized rock fractures to occur in groups. The fractures appear regularly, and are mainly a manifestation of the effects of the tectonic stress field.

Numerical simulations reveal that under the influence of NW-NNW-oriented tectonic compression and left-lateral compression deformation during the bending process of the fault, a relatively strong stress concentration phenomenon will form at the site, which corresponds to the characteristics of the geostress field indicated by the above phenomena and forms a localized tectonic feature. The phenomenon labeled ⑤ in Figure 9 was fully exposed at the site due to the excavation of the 318 highway, where the width of the bending section of the Zhuka fault was much larger than at other locations, and the compression fractures and deformation phenomena were very sufficient, showing local abnormal features.

The numerical simulation results show that the tectonic stress at the PDF03 site may be influenced by the movement of the Zhuka fault, causing the maximum principal stress to deflect towards the NNE direction (intersecting with the trend of the steeply inclined structural plane at a small angle) and increasing in value (see the numerical simulation results in Figure 10). This change creates the conditions and trends for strike-slip movement to occur on the structural plane in the downstream direction. However, before the valley developed, the burial depth was relatively large, which maintained a high level of normal stress perpendicular to the steeply inclined structural plane and suppressed the movement of the structural plane.

The most significant effect of valley evolution on the geostress of the rock mass on the opposite slope is the release of horizontal stress, i.e., a decrease in the normal stress perpendicular to the steeply inclined structural plane in the downstream direction. At this time, the influence of the tectonic stress parallel to the structural plane is relatively small, which means that during a certain stage of valley evolution, the unloading of the slope reduces the normal stress on the steeply inclined structural plane in the downstream direction, while causing the shear stress (the difference between the stresses parallel and perpendicular to the structural plane) on the surface to increase continuously, providing conditions for the movement of the structural plane. Obviously, due to the hardness and brittleness of the rock, the deformation capacity of the jointed parts of the structural plane (end, undulating section, intersection, etc.) cross each other. The movement and deformation along the structural plane tend to cause shear failure in these parts.

3.3. Influences Mechanism of the Zhuka Fault on the Geostress

3.3.1. Analysis Basis

The main tectonic stress in the engineering area is generally in the range of SWW-NNW and is in a continuously rotating state. However, the movement characteristics of the Zhuka fault and the bending section of the fault indicate the direction of the tectonic compression in the dam site area. Therefore, by using the observed movement characteristics of the fault at the site, it is possible to analyze the corresponding tectonic compression direction and the evolution process of the tectonic stress. Numerical simulations are used to investigate the relationship between the main tectonic stress direction and the different stages of fault movement and the stress conditions of the upper and lower rock masses, in order to understand the process of tectonic stress evolution.

The criteria for evaluating the reasonableness of the assumed tectonic compression direction in numerical simulations are as follows:

(a) The Zhuka fault and the bending section of the fault must exhibit characteristics of compression, and the later-formed bending section of the fault must exhibit thrust-twist characteristics.
(b) Compared with dextral thrust-twist, the stress distribution on both sides of the fault, especially the stress concentration zone, should correspond to the field observations in the case of the latest movement of the Zhuka fault being sinistral thrust-twist.

The most important purpose of the numerical simulation is to clarify the main tectonic stress direction in the dam site area. Therefore, the simulation process does not focus on the reasonableness of the numerical values. The assumptions of the numerical simulation are as follows:

(a) The analysis is conducted on a planar section, assuming that the self-weight stress component on this section reaches 20 MPa, which is equivalent to a depth of nearly 800 m.
(b) The initial geostress during the tectonic movement period is in a potential reverse fault state (consistent with the nature of the fault), and the ratio of the maximum, intermediate principal stresses, and vertical stress is 2:1.5:1, with the values of the maximum and intermediate principal stresses being 40 MPa and 30 MPa, respectively.
(c) Assuming that the direction of the maximum principal stress is 270° (EW), 300° (N60W), 330° (N30W), 30° (N30E), and 60° (N60E), respectively, under the above assumptions, the characteristics of fault movement (compression, dextral thrust-twist, sinistral thrust-twist) are analyzed under different conditions to clarify the direction of the tectonic stress in the dam site area at different stages.

Figure 11a shows a planar model constructed using FLAC3D (with one layer of elements in the vertical direction). The Zhuka fault dominates the NW direction, and the changes in the direction of the fault in the engineering area are accurately simulated to correctly reflect the relationship between the overall trend and local changes. The initial state of the numerical simulation does not consider the presence of the Zhuka fault, i.e., the fault is first treated as a complete rock mass, and then five different initial geostress fields are assigned for initial equilibrium calculation. The model reaches equilibrium by resetting the deformation to zero. At this time, the mechanical parameters of the fault are weakened, causing the stress imbalance at the fault location and resulting in fault movement and deformation, as well as changes in the stress state in the surrounding area. After the calculation reaches equilibrium, the fault movement state and stress distribution characteristics are examined. When they are fully consistent with the field observations, the corresponding main tectonic stress direction is considered to be sufficiently close to the tectonic compression direction in the dam site area.

3.3.2. Numerical Verification

Figure 11b shows the movement characteristics of the Zhuka fault under five different assumed conditions, with the lower right image magnifying the local effect in the dam site area corresponding to the tectonic compression direction of N30W. When the tectonic compression direction is assumed to be N30E and N60E, the Zhuka fault exhibits dextral strike-slip characteristics, consistent with the early stage of fault movement. That is to say, from the numerical simulation results, the RM dam site area of the Lancang River was once affected by a tectonic stress field of N30E~N60E, and this stage of tectonic stress was intense, consistent with the dominant movement characteristics of the Zhuka fault. Obviously, if the degree of tectonic movement in the later stage is relatively weak, this tectonic stress feature may be preserved and affect the current distribution of the geostress field. Under the other three assumed conditions, the Zhuka fault exhibits sinistral characteristics, representing the tectonic compression features corresponding to the later stage. According to the results of the field investigation, the early NE-directed compression and dextral tectonic compression were much stronger, forming the tectonic traces and fault movement phenomena in the dam site area.

Figure 11c shows the distribution characteristics of the maximum principal stress under the corresponding conditions (color-coded contour map), where the green background represents the initial stress conditions input for calculation, i.e., the assumed magnitude (40 MPa) under the burial depth conditions at that time. The orange and red areas with brighter colors represent stress increases caused by fault movement, while the blue areas represent stress reductions caused by stress release. The numerical simulation results show that during the early stage of N30E~N60E tectonic compression, stress relaxation occurred in the downstream of the dam site and the Rongqu section, indicating that the high-geostress phenomenon in the downstream of the dam site and the Rongqu gully was not the result of the early NE-directed tectonic compression.

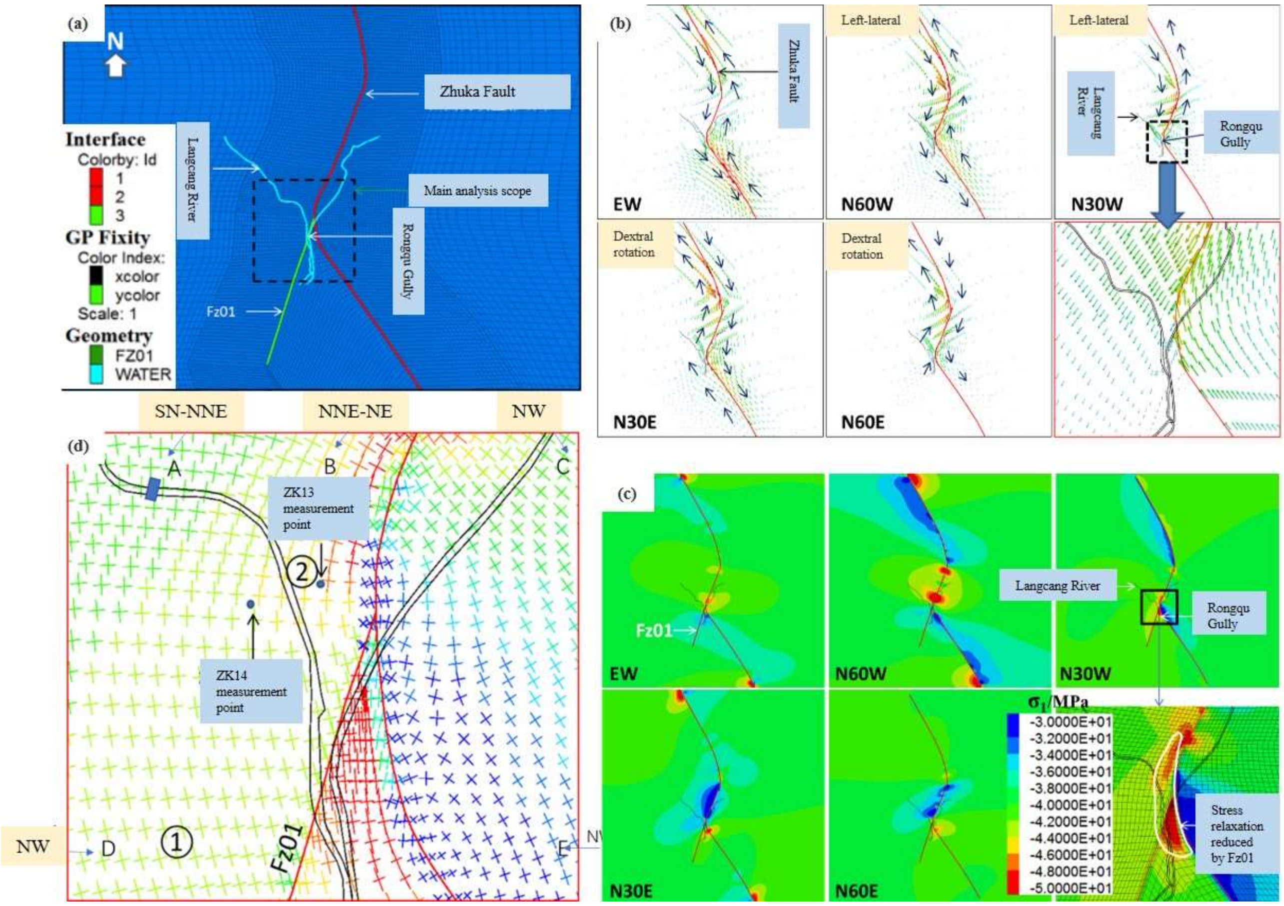

Figure 11. Numerical simulation model for the Zhuka fault: (**a**) the numerical model; (**b**) the numerical simulation results of the deformation trend of the fault under different compression directions (herein, the direction of the maximum principal stress is 270° (EW), 300° (N60W), 330° (N30W), 30° (N30E), and 60° (N60E), respectively); (**c**) the numerical simulation results of the stress contours of the fault under different compression directions (herein, σ_1 is the maximum principal stress); (**d**) the numerical simulation results of the stress field after the fault dislocation under N30W compression directions (herein, capital letters A, B, C, D and E represent the maximum principal stress direction); both ① and ② represent the point location.

Figure 11d shows the distribution characteristics of the tectonic stress vector in the dam site area during the later stage of N30W tectonic compression. The length and direction of the lines represent the stress vectors (the magnitude of the stress changes is also represented by colors, the same as in Figure 11c, to more clearly indicate stress concentration and relaxation). Obviously, in the right bank area downstream of the dam site and far away from the Zhuka fault (such as location ① in the figure), the main tectonic stress remains in the N30W direction, unaffected by the Zhuka fault. However, along the Lancang River from the dam site to the mouth of the Rongqu gully, the tectonic stress field is obviously affected by the Zhuka fault, the left bank mountainous area turns to the NNE-NE direction (location ② in the figure), and the right bank mountainous area is also slightly affected. It can be seen that the existence of the Zhuka fault significantly affects the distribution of tectonic stress in the dam site area, forming stress concentration and deflecting the direction of tectonic stress in the Rongqu ridge area, resulting in significant differences in tectonic stress conditions between the dam site and the middle dam site.

Obviously, in the later stage of valley evolution, the stress field in the middle and lower dam site areas will undergo different changes, resulting in differences in the current stress state.

The numerical simulation above shows that the sinistral thrust-twist movement characteristics of the bending section of the Zhuka fault in the later stage indicate a NW-N direction tectonic compression, consistent with the current tectonic compression direction indicated by surface movement velocity monitoring results and consistent with the tectonic stress field obtained by the source mechanism inversion in the dam site area (within the SWW-NNW range). From this perspective, the tectonic stress direction corresponding to the sinistral thrust-twist movement characteristics of the bending section of the Zhuka fault in the later stage is likely to be preserved in the downstream of the dam site area to the present day, i.e., the tectonic compression direction was NW-N before the river downcutting, and it still maintains this directional feature in the deep rock masses far away from the valley slope.

4. Discussions

In order to reveal the geostress in the study area, actual measurements of geostress were taken and compared with the numerical simulation results presented in this study. The layout of the geostress measurement points was determined based on the lithology exposed by the excavation of the open pit on site, and the relevant testing specifications. In consideration of the specific engineering conditions, intact or relatively intact rock areas were selected in the dam site area, and test points were arranged where there was no developed fissure. The hydraulic fracturing method was used in this study to measure the geostress and analyze the relationship between maximum principal stress (σ_1) and vertical depth (h). In order to facilitate the analysis of the variation of geostress with depth in both the riverbed and slope boreholes, the geostress levels measured in the riverbed and slope boreholes were separately statistically analyzed, as shown in Figure 12.

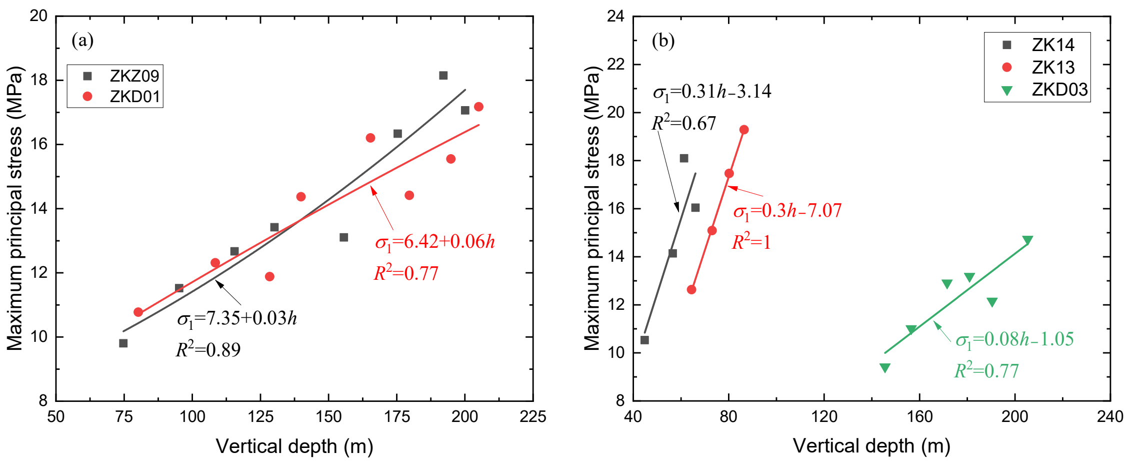

Figure 12. Relationship curves between maximum horizontal principal stress and vertical depth: (**a**) borehole at riverbed; (**b**) borehole at reservoir bank slope. Note: σ_1 is the maximum principal stress; h is the vertical depth; R^2 is the determination coefficient.

A large amount of test data are generated using the hydraulic fracturing method. Statistical analysis indicated that the maximum horizontal principal stress in the riverbed boreholes increased significantly with vertical depth, with a tendency to slow down after 190 m, and the stress value ranged from 17 MPa to 18 MPa, as shown in Figure 12a. The maximum horizontal principal stress in the riverbed borehole ZKZ09 was found to be approximately a linear function of vertical depth, with a fitting function of $\sigma_1 = 7.35 + 0.03$ h. The maximum horizontal principal stress in riverbed borehole ZKD01 was found to be approximately a linear function of vertical depth, with a fitting function of $\sigma_1 = 6.42 + 0.06$ h.

Based on this good correlation, it is possible to predict the maximum horizontal principal stress in the region.

In Figure 12b, the distribution of the maximum horizontal principal stress in the slope boreholes was relatively scattered, and was related to the terrain conditions and the development of unloading. However, the values were mainly distributed between 10 MPa and 20 MPa, with a minimum of 9.45 MPa and a maximum of 19.29 MPa. The trend of increasing stress values with depth was also evident from the analysis of individual borehole data. The maximum horizontal principal stress in slope borehole ZK13 was found to be approximately a greatly linear function of vertical depth, with a fitting function of $\sigma_1 = 0.3\ h - 7.07$. For boreholes ZK14 and ZKD03, the fitted results are worse than those of ZK13. This means that there are outliers in these data, which may be errors during the measurement process. Nevertheless, the slopes of the fitted curves in ZK14 and ZK13 are basically consistent. This indicates that the growth rate of the principal stress remains consistent as the vertical depth increases in both boreholes.

In summary, the geostress measurements in the dam area exhibit the following characteristics:

(a) The occurrence of pie-shaped rock cores, slices, and damaged rock masses in some areas indicate the presence of high-geostress or poor-geostress conditions in this area.
(b) The overall maximum principal stress in the hub area is in the NE-NEE direction, with some local variations in the NWW direction. According to the stress relief method based on borehole deformation analysis, the dip direction is S, and the dip angle varies between 13° and 57°. The dip angle of the maximum principal stress in the underground power plant area is relatively flat, ranging from 9° to 21°.
(c) The overall geostress in the hub area increases with depth. In the shallow part, the geostress is relatively low, with a maximum principal stress value of around 10 MPa due to the unloading of the rock mass. In the depth range of 50 m to 220 m, the geostress values are between 10 MPa and 20 MPa (increasing with depth), which is considered moderate geostress. In the deep part (such as the underground power plant area, with a depth of 400 m to 600 m), the geostress values are above 22 MPa to 28 MPa, with a rock strength to maximum principal stress ratio of 2.5, indicating a high-geostress zone.
(d) In the low elevation area of the dam site, a clear "slicing" phenomenon can be observed at a horizontal depth of 150 m to 230 m, and a "rock cake" phenomenon can be seen in some riverbed boreholes at a vertical depth of 50 m to 100 m. However, the on-site geostress test results show that the phenomenon of increasing geostress near the riverbed in the horizontal and vertical directions is not significant, indicating that the phenomenon of "stress pockets" is not obvious. The main reason for this is the development of structural planes in the riverbed and slope rock masses. In addition, as the elevation increases, the rock mass of the slope undergoes strong weathering and unloading, which releases the geostress, and thus, there is no obvious "stress pocket" near the riverbed and slope.

5. Conclusions and Prospect

5.1. Conclusions

(1) The Zhuka fault breccia zone is dominated by tectonic breccia, and breccia, brecciated tuff, and fault gouge are also well developed. Based on further investigations of the site area, the main evidence for the inactivity of the Zhuka fault can be determined. The dislocation characteristics of the Zhuka fault also reveal the features of tectonic activity in the dam site area.
(2) The geostress concentration is observed and verified using the numerical simulation. The sinistral thrust-twist movement characteristics of the bending section of the Zhuka fault in the later stage indicate a NW-N direction tectonic compression, consistent with the current tectonic compression direction indicated by surface movement velocity

monitoring results and consistent with the tectonic stress field obtained via the source mechanism inversion in the dam site area.

(3) The hydraulic fracturing method was used in this study to measure the geostress and analyze the relationship between the maximum principal stress and the vertical depth. The maximum horizontal principal stress in the riverbed boreholes was found to be approximately a linear function of vertical depth, while the maximum horizontal principal stress in slope boreholes was found to be approximately an exponential function of vertical depth.

5.2. Guiding Significance for Engineering

Deformation and failure phenomena can often be observed at the surface of faults, which have certain impacts on the distribution of the stress field. Investigating these characteristics and their influence on the stress field is of significant importance in the field of engineering.

Firstly, research on the deformation and failure characteristics of faults can reveal the movement mechanisms and deformation patterns of faults within the Earth's crust. Analyzing the deformation features of faults enables us to understand information such as accumulated displacement, slip rate, and slip direction, providing a basis for earthquake prediction and geological hazard assessment. Additionally, studying the characteristics of fault failure can unveil the processes and mechanisms of fault rupture, serving as a foundation for earthquake rupture simulation and source parameter inversion.

Secondly, the investigation of fault deformation and failure characteristics contributes to our understanding of the evolution and distribution patterns of stress states in the Earth's crust. The deformation and failure processes of faults are the result of stress release and redistribution in the crust. By analyzing the deformation features of faults, it is possible to infer the variations in the local stress field. Understanding the evolution and distribution patterns of the stress field is crucial for underground engineering design and geological hazard prevention, providing a basis for determining excavation and support schemes and evaluating engineering stability.

Thirdly, research on fault deformation and failure characteristics can provide a basis for assessing fault activity and conducting seismic risk analysis. Through the observation and analysis of fault deformation features, the activity of faults can be determined, and the potential hazards of earthquakes can be evaluated. This is of great significance for seismic risk analysis, earthquake damage assessment, and the establishment of earthquake monitoring and early warning systems. Furthermore, studying fault deformation and failure characteristics can also provide scientific guidance for post-earthquake disaster assessment and reconstruction efforts.

This study provides valuable insights into geostress concentration and its implications for sustainable development in the Sichuan–Tibet region. The findings highlight the importance of considering the geotechnical risks associated with faults and geostress distribution in infrastructure projects. The observed high-geostress damage on the downstream slope of the lower dam site emphasizes the need for site selection that accounts for geostress concentration outside the fault zone. These findings will contribute to the advancement of sustainable engineering practices and aid in the decision-making processes of infrastructure development projects in the region.

Author Contributions: Methodology, S.W.; software, D.H. and H.Z.; validation, T.W.; formal analysis, D.H.; investigation, S.W. and D.H.; resources, D.H.; writing—review and editing, D.H., T.W. and W.H.; visualization, S.W. and D.H.; supervision, T.W. All authors have read and agreed to the published version of the manuscript.

Funding: The work was funded by the Science and Technology Program of Tibet Autonomous Region (XZ202301YD0034C, XZ202202YD0007C); the National Natural Science Foundation of China (No. 42002268); the Open Fund of Badong National Observation and Research Station of Geohazards (No. BNORSG-202204); and the Open Foundation of Engineering Research Center of Rock–Soil Drilling and Excavation and Protection, Ministry of Education (202211).

Institutional Review Board Statement: Not applicable.

Informed Consent Statement: Not applicable.

Data Availability Statement: The datasets generated during and/or analyzed during the current study are available from the corresponding author on reasonable request.

Acknowledgments: The author thanks Mengming Chen for his efforts in the drawing process.

Conflicts of Interest: The authors declare no conflict of interest.

References

1. He, X.; Xu, C.; Qi, W.; Huang, Y.; Cheng, J.; Xu, X.; Yao, Q.; Lu, Y.; Dai, B. Landslides Triggered by the 2020 Qiaojia Mw5.1 Earthquake, Yunnan, China: Distribution, Influence Factors and Tectonic Significance. *J. Earth Sci.* **2021**, *32*, 1056–1068. [CrossRef]
2. Ning, Y.B.; Tang, H.; Smith, J.V.; Zhang, B.; Shen, P.; Zhang, G. Study of the in situ stress field in a deep valley and its influence on rock slope stability in Southwest China. *Bull. Eng. Geol. Environ.* **2021**, *80*, 3331–3350. [CrossRef]
3. Wang, S.Y.; Zhou, R.; Liang, M.; Liu, S.; Liu, N.; Long, J. Co-Seismic Surface Rupture and Recurrence Interval of Large Earthquakes along Damaoyaba-Litang Segment of the Litang Fault on the Eastern Margin of the Tibetan Plateau in China. *J. Earth Sci.* **2021**, *32*, 1139–1151. [CrossRef]
4. Ha, G.; Liu, J.; Ren, Z.; Zhu, X.; Bao, G.; Wu, D.; Zhang, Z. The Interpretation of Seismogenic Fault of the Maduo Mw 7.3 Earthquake, Qinghai Based on Remote Sensing Images—A Branch of the East Kunlun Fault System. *J. Earth Sci.* **2022**, *33*, 857–868. [CrossRef]
5. Chen, Z.Q.; Zhou, Z.; He, C.; Jiang, C.; Wang, B.; Li, T. Influence of faults on the geo-stress field distribution and damage evolution mechanism of fracture zones. *Bull. Eng. Geol. Environ.* **2023**, *82*, 173. [CrossRef]
6. Wu, S.Y.; Hu, D.R.; Wen, T. Special Characteristics and Stability Analysis of Bank Slope Deposits with Special Geotechnical Structures in High and Cold Valleys. *Sustainability* **2023**, *15*, 6090. [CrossRef]
7. Chen, G.I.; Bartholomew, M.; Liu, D.; Cao, K.; Feng, M.; Wang, D. Paleo-Earthquakes along the Zheduotang Fault, Xianshuihe Fault System, Eastern Tibet: Implications for Seismic Hazard Evaluation. *J. Earth Sci.* **2022**, *33*, 1233–1245. [CrossRef]
8. Wen, T.; Hu, Z.; Wang, Y.K.; Zhang, Z.H. Variation Law of Air Temperature of a High-Geotemperature Tunnel during the Construction. *Lithosphere* **2021**, *2021*, 2541884. [CrossRef]
9. Wen, T.; Hu, Z.; Wang, Y.; Zhang, Z.; Sun, J. Monitoring and Analysis of Geotemperature during the Tunnel Construction. *Energies* **2022**, *15*, 736. [CrossRef]
10. Zhao, B.; Su, L.J.; Wang, Y.S.; Li, W.L.; Wang, L.J. Insights into some large-scale landslides in southeastern margin of Qinghai-Tibet Plateau. *J. Rock Mech. Geotech. Eng.* **2023**, *15*, 1960–1985. [CrossRef]
11. Fang, H.H.; Sang, S.X.; Wang, J.L.; Liu, S.Q.; Ju, W. Simulation of Paleotectonic Stress Fields and Distribution Prediction of Tectonic Fractures at the Hudi Coal Mine, Qinshui Basin. *Acta Geol. Sin.* **2017**, *91*, 2007–2023. [CrossRef]
12. Jiang, L.; Qiu, Z.; Wang, Q.; Guo, Y.; Wu, C.; Wu, Z.; Xue, Z. Joint development and tectonic stress field evolution in the southeastern Mesozoic Ordos Basin, west part of North China. *J. Asian Earth Sci.* **2016**, *127*, 47–62. [CrossRef]
13. Li, P.; Cai, M.F.; Miao, S.J.; Guo, Q.F. New insights into the current stress field around the Yishu fault zone, eastern China. *Rock Mech. Rock Eng.* **2019**, *52*, 4133–4145. [CrossRef]
14. Li, X.L.; Chen, S.J.; Wang, S.; Zhao, M.; Liu, H. Study on In Situ Stress Distribution Law of the Deep Mine: Taking Linyi Mining Area as an Example. *Adv. Mater. Sci. Eng.* **2021**, *2021*, 5594181. [CrossRef]
15. Wu, Z.H.; Tang, M.; Zuo, Y.; Lou, Y.; Wang, W.; Liu, H.; Sun, W. Acoustic emission-based numerical simulation of tectonic stress field for tectoclase prediction in shale reservoirs of the northern Guizhou area, China. *Energy Geosci.* **2022**, *3*, 436–443. [CrossRef]
16. Yin, S.; Ding, W.; Zhou, W.; Shan, Y.; Xie, R.; Guo, C.; Cao, X.; Wang, R.; Wang, X. In situ stress field evaluation of deep marine tight sandstone oil reservoir: A case study of Silurian strata in northern Tazhong area, Tarim Basin, NW China. *Mar. Pet. Geol.* **2017**, *80*, 49–69. [CrossRef]
17. Zeng, W.T.; Ding, W.; Zhang, J.; Zhang, Y.; Guo, L.; Jiu, K.; Li, Y. Fracture development in Paleozoic shale of Chongqing area (South China). Part two: Numerical simulation of tectonic stress field and prediction of fractures distribution. *J. Asian Earth Sci.* **2013**, *75*, 267–279. [CrossRef]
18. Zhang, Q.; Qu, W.; Wang, Q.; Peng, J.; Drummond, J.; Li, Z.; Lin, Q. Analysis of Present Tectonic Stress and Regional Ground Fissure Formation Mechanism of the Weihe Basin. *Surv. Rev.-Dir. Overseas Surv.* **2011**, *43*, 382–389. [CrossRef]
19. Zhang, Z.G.; Qin, Y.; You, Z.J.; Yang, Z.B. Distribution Characteristics of In Situ Stress Field and Vertical Development Unit Division of CBM in Western Guizhou, China. *Nat. Resour. Res.* **2021**, *30*, 3659–3671. [CrossRef]

20. Augustinus, P.C. Glacial valley cross-profile development: The influence of in situ rock stress and rock mass strength, with examples from the Southern Alps, New Zealand. *Geomorphology* **1995**, *14*, 87–97. [CrossRef]
21. Martinez-Diaz, J.J. Stress field variation related to fault interaction in a reverse oblique-slip fault: The Alhama de Murcia fault, Betic Cordillera, Spain. *Tectonophysics* **2002**, *356*, 291–305. [CrossRef]
22. Kattenhorn, S.A.; Marshall, S.T. Fault-induced perturbed stress fields and associated tensile and compressive deformation at fault tips in the ice shell of Europa: Implications for fault mechanics. *J. Struct. Geol.* **2006**, *28*, 2204–2221. [CrossRef]
23. Veloso, E.E.; Gomila, R.; Cembrano, J.; González, R.; Jensen, E.; Arancibia, G. Stress fields recorded on large-scale strike-slip fault systems: Effects on the tectonic evolution of crustal slivers during oblique subduction. *Tectonophysics* **2015**, *664*, 244–255. [CrossRef]
24. Xie, H.; Li, Z.; Yuan, D.; Wang, X.; Su, Q.; Li, X.; Wang, A.; Su, P. Characteristics of Co-Seismic Surface Rupture of the 2021 Maduo Mw 7.4 Earthquake and Its Tectonic Implications for Northern Qinghai–Tibet Plateau. *Remote Sens.* **2022**, *14*, 4154. [CrossRef]
25. Li, G.; Hu, Y.; Li, Q.-B.; Yin, T.; Miao, J.-X.; Yao, M. Inversion Method of In-situ Stress and Rock Damage Characteristics in Dam Site Using Neural Network and Numerical Simulation—A Case Study. *IEEE Access* **2020**, *8*, 46701–46712. [CrossRef]
26. Ren, Q.Q.; Jin, Q.; Feng, J.W.; Li, M.P. Simulation of stress fields and quantitative prediction of fractures distribution in upper Ordovician biological limestone formation within Hetianhe field, Tarim Basin, NW China. *J. Pet. Sci. Eng.* **2019**, *173*, 1236–1253. [CrossRef]
27. Fang, K.; Zhang, J.; Tang, H.; Hu, X.; Yuan, H.; Wang, X.; An, P.; Ding, B. A quick and low-cost smartphone photogrammetry method for obtaining 3D particle size and shape. *Eng. Geol.* **2023**, *322*, 107170. [CrossRef]